Transitions between mode-locked and noise-like pulsed states in a multimode fiber laser

KAROLINA STEFAŃSKA[1, †], VITTORIO CECCONI[1, †,*], KATARZYNA KRUPA[2], LUYAO ZHOU[3], JOSE ALFREDO ALVAREZ-CHAVEZ[4], STUART G. MURDOCH[5,6], FABIO MANGINI[1,7], AND STEFAN WABNITZ[1]

[1] *Department of Information Engineering, Electronics and Telecommunications, Sapienza University of Rome, 00184 Rome, Italy*
[2] *Institute of Physical Chemistry, Polish Academy of Sciences, 01-224 Warsaw, Poland*
[3] *College of Communication Engineering, Jilin University, Changchun 130012, China*
[4] *The Hague University of Applied Sciences, Lectoraat Fotonica, Rotterdamseweg 137, 2628AL Delft, The Netherlands*
[5] *Department of Physics, University of Auckland, Auckland 1010, New Zealand*
[6] *The Dodd-Walls Centre for Photonic and Quantum Technologies, Auckland, New Zealand*
[7] *Department of Engineering, Niccolo Cusano University, Via Don Carlo Gnocchi 3, 00166 Rome, Italy*
† *These authors contributed equally to this work.*
* *vittorio.cecconi@uniroma1.it*

Compiled September 1, 2026

We experimentally demonstrate transitions between stably mode-locked and noise-like pulse states in a Ytterbium-doped fiber laser controlled by adjusting the level of intracavity spectral filtering. In both regimes, Kerr spatial self-cleaning provides high-quality output beams. By using cavities with different lengths of graded-index fiber, we show that, in the mode-locked regime, a proper balance between chromatic and modal dispersion maximizes pulse compressibility. We compress 2.1-kW, 6.7-ps pulses down to 170 fs using an external grating pair, in good agreement with numerical simulations.

http://dx.doi.org/10.1364/ao.XX.XXXXXX

Passive mode-locked fiber lasers provide a reliable source of ultrashort pulses—from femtoseconds to picoseconds—making them essential tools in telecommunications, biomedical imaging, and material processing [1]. These pulses emerge from a balance between dispersion, nonlinearity, gain, and loss [2], defining a fundamentally dissipative nonlinear system [3]. Among the various passive mode-locking mechanisms, nonlinear polarization evolution (NPE) remains one of the most widely used, permitting both stable mode-locked [4] and noise-like [5] regimes. Such regimes can be accessed simply by adjusting the intracavity polarization controllers or the pump power. In parallel, within the fiber optics community, multimode graded-index fibers (GIF) have attracted widespread interest due to their unique nonlinear response, large mode area, and high damage threshold. Their low modal dispersion and periodic self-imaging enable rich spatiotemporal dynamics, including, most importantly for this work, beam self-cleaning [6, 7]. Building on these two research directions, multimode cavities incorporating NPE have recently emerged as a powerful platform to explore spatiotemporal mode-locking [8, 9]. Experiments combining multimode GIF and Ytterbium-doped gain fibers have demonstrated stable spatiotemporal mode-locked states, soliton molecules, and noise-like states [10–12], highlighting the versatility of NPE in the multimode operation regime. In these systems, Kerr-induced beam self-cleaning plays a crucial role by redirecting energy from higher-order modes into the fundamental mode, improving beam quality in both mode-locked and noise-like regimes [13–15]. As a result, NPE-based multimode fiber laser cavities have become a testbed for exploring nonlinear multimode dynamics, simultaneously providing practical advantages such as high pulse energy, tunable spectral and temporal shaping, and improved beam quality.

In this work, we investigate an all-normal dispersion spatiotemporal mode-locked Yb-doped fiber laser cavity based on a combination of few-mode fibers and multimode graded-index fibers. We reveal that a disordered noise-like pulse regime can be transformed into an ordered stable mode-locked state by suitably narrowing the bandwidth of an intracavity spectral filter. Moreover, we demonstrate the existence of an optimal balance between chromatic and modal dispersion, which permits us to maximize pulse compressibility by an external grating pair.

Our all-normal dispersion fiber cavity (Fig. 1) is pumped by a pair of 976 nm multimode laser diodes, coupled through 100 μm-core fibers into a pump combiner, for a total of up to 5 W pump power. The cavity itself is composed of Yb-doped fiber (YDF, 3.4 m, Liekki Yb1200-10/125DC), passive few-mode fiber (FMF, total of 4.9 m, Thorlabs SMF28e), multimode graded-index fiber (GIF, varied lengths, Thorlabs GIF50e), passive double-clad fiber (DCF, 3.4 m, Liekki Passive-10/125DC), and a free-space section with waveplates, a polarizing beamsplitter cube, a Faraday isolator (Newport ISO-FRDY-08-1064-N), and a removable bandpass spectral filter centered at 1064 nm (Thorlabs FLH1064-3 and FLH1064-10). Our simulations show that, in this configuration, the GIF section of the cavity is where modal dispersion, nonlinear mode coupling, and periodic self-imaging primarily enable spatiotemporal dynamics; whereas the remaining fiber segments mainly contribute gain and chromatic dispersion. By carefully adjusting the waveplates and fiber polarization con-

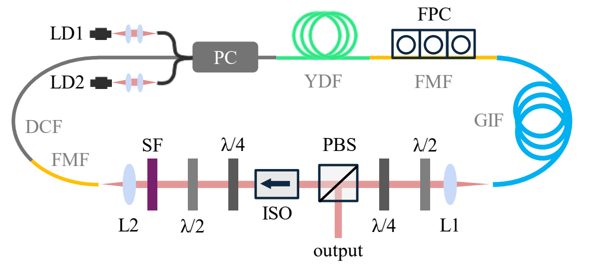

Fig. 1. Fiber laser setup with: LD – laser diodes; PC – pump combiner; FPC – fiber polarization controller; L - lenses; $\lambda/2$ – half-wave plate; $\lambda/4$ – quarter-wave plate; PBS – polarizing beamsplitter cube; ISO – isolator; SF – spectral filter.

trollers placed on the first segment of the FMF, we were able to obtain pulsed operation for each configuration. Throughout this work, pulse durations are retrieved by assuming a Gaussian temporal profile, which provides a consistent reference for comparing different operating regimes. All optical spectra reported in the following are normalized to their maximum value, in order to allow for a direct comparison of their profiles.

We first employed 5.2 meters of GIF and a 3-nm bandwidth spectral filter. The cavity characterization with (and without) the spectral filter in the free-space section is shown in Fig. 2(c-g,k-m) and Fig. 2(a-b,h-j), respectively. In both cases, we reached a pulsed state of operation by suitably adjusting the polarization controllers and waveplates with the same pump power of 2.8 W. The smooth broadband output spectrum from the no-filter cavity (Fig. 2(a)) is in stark contrast with the fine spectral structure that is present in the spectrum from the cavity with the 3 nm spectral filter present (Fig. 2(c)). This suggests that, in the absence of the bandpass filter, the laser operates in a chaotic noise-like state, as opposed to the stable mode-locked regime which is observed when the filter is present [16]. This is confirmed by our measured autocorrelation traces: the no-filter cavity autocorrelation (Fig. 2(b)) shows a sharp peak on top of a broad $\sim$ 30 ps background, confirming its noise-like origin. By contrast, the autocorrelation of the 3-nm filter cavity (Fig. 2(d)) shows a single clean trace, indicating that stable mode-locking occurs. The retrieved pulse duration is 6.74 ps. We were able to compress these pulses down to 170 fs by using an external Treacy grating compressor [17], as shown in Fig. 2(e). The coherence of the mode-locked state was confirmed by the measured radio-frequency spectrum (Fig. 2(g)) with a high signal-to-noise ratio of 56.5 dB. The retrieved repetition rate of 11.96 MHz corresponds to a total cavity length of 16.9 m. The average power measured at the laser output is 280 mW in the noise-like state, corresponding to a pulse energy of 23.4 nJ, while in the mode-locked state the average power reaches 170 mW, corresponding to a pulse energy of 14.2 nJ and a peak power of 2.1 kW (before compression).

Interestingly, both cavities (with or without bandpass filter) show clear evidence of beam self-cleaning at the laser output when operating in a pulsed regime, compare Figs. 2(i-j) for the no-filter cavity (Fig. 2(l-m) for the 3-nm-filter cavity) before and after reaching pulsed operation. We experimentally determined the quality of the output beam by measuring $M_x^2 \approx M_y^2 \approx 1.5$ for both pulsed modes of operation (Fig. 2(h,k)). These results provide a clear quantitative signature of beam self-cleaning, which we attribute to the high pulse peak power in both regimes.

To gain more insight on the pulse propagation dynamics in

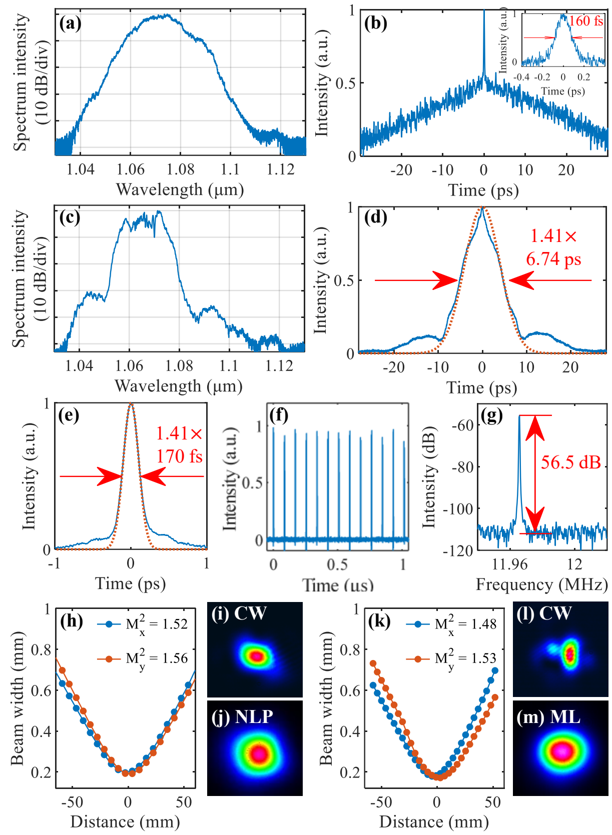

Fig. 2. Noise-like (a-b,h-j) and mode-locked (c-g,k-m) pulses in the cavity with 5.2 meters of GIF. Measured output spectra (a, c) and autocorrelation traces (b, d). Measured autocorrelation trace of the compressed pulse (e), pulse train (f) and radio-frequency spectrum (g) of the mode-locked cavity. Output near-field images for CW (i,l) and pulsed (j,m) state; and measured M^2 of the pulsed beam (h,k).

our cavity, we performed extensive numerical simulations of spatiotemporal mode locking by adapting the numerical solver proposed in [8]. We evaluated the nonlinear pulse propagation in the gain fiber and in the passive FMF, DCF, and GIF, by considering for simplicity only the first six linearly polarized modes in the GIF, and the first three modes in the FMF and the gain fiber. After the GIF segment, we assumed that the combination of the beam splitter and nonlinear polarization acts as a fast saturable absorber, and considered a Gaussian spectral filter with 3 nm bandwidth. A stable mode-locking regime was reached after 17 iterations: the corresponding results are outlined in Fig. 3. As can be seen, the pulse duration steadily increases during propagation, reaching 5.1 ps at FWHM at the laser output after the GIF. The calculated transform-limited pulse duration is 125 fs, and when dechirped by a simulated grating pair, it is 140 fs. Those numerical results show a good agreement with the measured pulse duration, and confirm the very good degree of compression that is achieved in our experiments. During propagation around the cavity, the simulated spectrum undergoes a 5-fold spectral broadening, reaching the FWHM bandwidth of 14.6 nm after the GIF. The simulated output spectrum plotted in blue in Fig. 3(d) corresponds very well to that observed in the experiments, plotted in red (also presented in Fig. 2(c) in log scale), showing that a successful reproduction of the experimental mode-locking could be achieved in our numerical

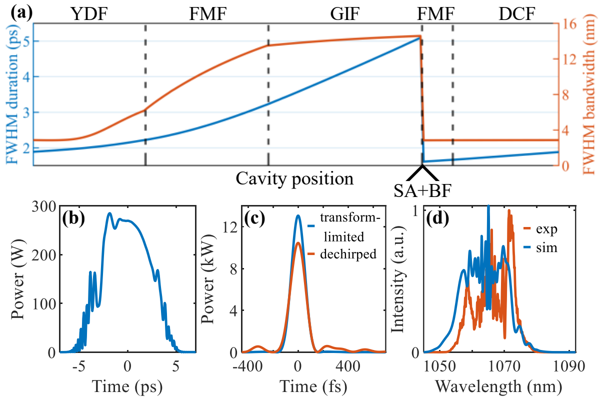

Fig. 3. Simulated periodic evolution of pulse duration and spectral bandwidth in the cavity (a) with SA - saturable absorber; BF - bandpass spectral filter. Simulated output pulse (b), calculated transform-limited pulse (c) and output spectrum (d). Numerical spectrum is compared to the experimental spectrum from Fig. 2(c) plotted in linear scale.

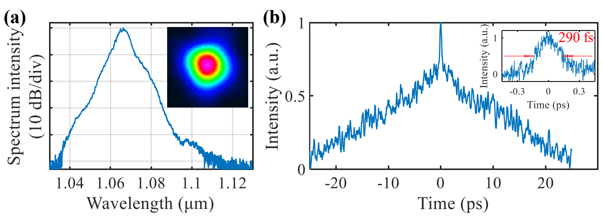

Fig. 4. Noise-like pulses in the cavity with 5.2 meters of GIF with 10-nm bandwidth spectral filter. Measured output spectrum (a) and autocorrelation trace (b) with the corresponding narrow peak atop the pedestal (inset). Inset of (a) shows output beam near-field for pulsed state.

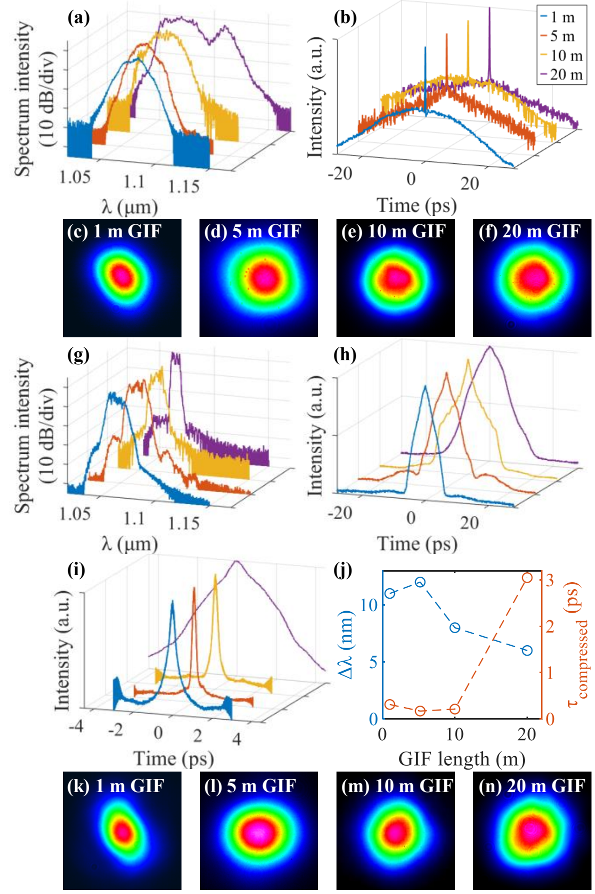

Fig. 5. Noise-like and mode-locked states in cavities with different lengths of GIF. Measured spectra (a)/(g), autocorrelation traces (b)/(h), and near-field images of the output pulsed beam (c-f)/(k-n) in the cavities without/with the bandpass spectral filter. Autocorrelation traces of compressed pulses (i) and analysis of spectral bandwidth and compressed pulse duration (j) in the mode-locked cavities.

simulations. Although the numerical model includes a limited number of modes and idealized lumped elements, it captures the essential interplay between dispersion, nonlinearity, and spectral filtering that governs the stable mode-locking mechanism.

In the next step, we experimentally studied the cavity operation with a weaker intra-cavity spectral filtering, by inserting a 10 nm bandpass filter in the free-space section. In this case we observed the generation of a smooth triangular-shaped spectrum, which corresponds to an autocorrelation trace with a broad pedestal and a narrow 290-fs peak, shown in Fig. 4. Due to the presence of a narrow peak in the autocorrelation trace, the smooth spectral profile and the reduced temporal coherence indicate that in this regime the laser emission remains noise-like, rather than stably mode-locked. Therefore, consistent with the established essential role of spectral filtering in normal-dispersion fiber lasers [18, 19], we conclude that sufficiently strong spectral filtering is required to achieve stable spatiotemporal mode-locking. We note that transitions between different regimes induced by spectral filtering have also been reported in Refs. [20, 21]. Based on this, a 3-nm filter was employed in our subsequent studies.

Next, we investigated the dynamics of pulse emission in the cavities with the same design, but with different lengths of GIF: specifically: 1, 5.2, 10, and 20 meters. This allowed us to vary the relative contributions of chromatic and modal dispersion in our multimode laser cavity. In the 5.2-m-GIF cavity, the combination of fiber chromatic dispersion, total cavity length, and pulse spectral bandwidth results in a net group delay of approximately −5.6 ps per round trip. Remarkably, this delay has a magnitude comparable to that associated with modal dispersion, which is approximately 5.2 ps per round trip, when considering the first 10 modes of GIF. This condition—namely operating a multimode cavity with same order of modal and chromatic dispersion—satisfies the criterion for achieving STML as it was suggested in Ref. [8]. By varying the length of the multimode fiber away from the optimal length of 5.2 m, we could explore regimes where either chromatic or modal dispersion dominates: for the 1-m GIF, chromatic dispersion dominates by a factor of 4, whereas for the 20-m GIF, modal dispersion dominates by a factor of 4.

In each cavity, we verified the possibility of achieving mode-locked operation when having the 3-nm bandpass filter present or removed from the free-space section. The pump power was maintained at around 3 W. Our investigation, summarized in Fig. 5, confirms the trend noted in the previous experiments. Without the spectral filter, we always observed noise-like pulse generation, as evidenced by the broad smooth spectra shown in

Fig. 5(a) and the autocorrelation traces featuring a sharp peak atop a broad pedestal shown in Fig. 5(b). The output spectrum of the 20 m GIF cavity has a component centered at 1110 nm, indicating a significant role of Raman scattering occurring during the relatively long roundtrip of the pulse.

In contrast, after reintroducing the spectral filter in the cavity, we achieved a mode-locked state for each length of GIF. The measured output spectra and autocorrelation traces are shown in Fig. 5(g) and (h), respectively. In each case, the spectrum exhibits characteristic rapidly varying oscillations which indicate the occurrence of spatiotemporal mode-locking [15]. The dependence of spectral width (at FWHM) vs GIF length is analyzed in Fig. 5(j). The spectrum reaches the largest bandwidth of 12 nm (FWHM) in the 5.2-m GIF cavity, and it is only half as broad in the longest 20-m GIF cavity. The output pulse duration, summarized in Table 1, gradually increases with the cavity length, from 5.2 ps (1 m GIF) up to 9.8 ps (20 m GIF). Interestingly, the cavity length has a significant impact on the ability to compress the output pulses; see Fig. 5(i) and orange markers in Fig. 5(j). The strongest compression is achieved in a cavity with a 5.2-m-long GIF, which, as expected, also has the broadest measured spectrum. Deviations from this GIF length lead to accumulation of the effects of dispersion - either chromatic or intermodal - thus increasing the influence of higher-order dispersion terms, thereby limiting the achievable pulse compression. The performance of the cavities also differs in terms of radio-frequency spectrum, as summarized in Table 1. Once more, the 5.2-m-GIF cavity stands out as the best among those that we tested, as it exhibits the highest signal-to-noise ratio. We also note that the measured repetition rates correspond to the total length of the cavity in each case.

Finally, we observed that beam self-cleaning is obtained in both noise-like and mode-locked pulsed regimes. This indicates that, while beam-cleaning is not sufficient to ensure spatiotemporal mode-locking, it is consistently associated with the high peak powers of the pulsed states. The captured near-field images presented in Fig. 5 show, for each investigated cavity, the emergence of a clean output beam when a pulsed mode of operation is reached. The recorded profiles are complemented with the M^2 characterization of the output beam, yielding satisfactory results, which are compiled in Table 1.

In conclusion, we present a systematic study of transitions between mode-locked and noise-like pulse states in a Yb-based multimode fiber laser. By controlling the bandwidth of the intracavity filter, we explore the transition between two separate emission regimes, which can be associated with a spatiotemporal intermittency dynamics [22]. The laser output exhibits a high-quality beam profile coupled with high-energy pulses and a broadband spectrum. We have experimentally demonstrated that reaching an optimal pulse compression requires a careful control of the GIF length in order to minimize the influence of higher-order dispersion. Beyond physics, the investigated transition pathway can be of great interest for new biomedical applications such as optical coherence tomography, where both high peak power and improved imaging performance are advantageous [23, 24].

Table 1. Characterization of cavities with different GIF lengths, with: L_{GIF} - GIF length; τ - pulse duration for the mode-locked cavity; f_{rep} - repetition rate of the cavity; RF SNR - signal-to-noise ratio of the radio-frequency spectrum for the mode-locked cavity; $M^2_{x/y}$ - M^2 measured in two orthogonal directions for NLP - noise-like cavity; ML - mode-locked cavity. For reference, $M^2_x = M^2_y = 2.14$ in the CW state for the 20-m cavity.

L_{GIF} (m)	τ (ps)	f_{rep} (MHz)	RF SNR (dB)	M^2_x / M^2_y for NLP	M^2_x / M^2_y for ML
1	5.2	15.9	45.6	1.61/1.16	1.33/1.39
5.2	6.7	11.96	56.5	1.52/1.56	1.48/1.53
10	7.5	9.40	40.2	1.40/1.52	1.70/1.53
20	9.8	6.42	23.8	1.64/1.58	1.40/1.46

Funding. European Innovation Council (Grant no. 101185664). S.G. Murdoch acknowledges a Sapienza visiting fellowship. We acknowledge Narodowe Centrum Nauki NCN (OPUS25 2023/49/B/ST7/01482) and Narodowa Agencja Wymiany Akademickiej NAWA (Canaletto BPN/BIT/2024/1/00035 and the Italian Ministry of Foreign Affairs and International Cooperation (MAECI) Grant no. M00357.

Acknowledgment. The authors thank Prof. T. Scopigno and Prof. D. Modotto for lending us some optical components and Dr D. S. Kharenko and G. Fu for helpful discussions.

Disclosures. The authors declare no conflicts of interest.

Data availability. Data underlying the results presented in this paper are not publicly available at this time but may be obtained from the authors upon reasonable request.

Supplemental document. See Supplement 1 for supporting content.

REFERENCES

1. M. E. Fermann and I. Hartl, Nat. Phot. **7**, 868 (2013).
2. P. Grelu and N. Akhmediev, Nat. Phot. **6**, 84 (2012).
3. E. Vanin, A. Korytin, A. Sergeev, *et al.*, Phys. Rev. A **49**, 2806 (1994).
4. V. J. Matsas, T. P. Newson, D. J. Richardson, and D. N. Payne, Electron. Lett. **28**, 1391 (1992).
5. Y. Meng, O. Ougrige, F. Bessin, *et al.*, Appl. Phys. Lett. **124**, 201104 (2024).
6. K. Krupa, A. Tonello, B. M. Shalaby, *et al.*, Nat. Phot. **11**, 237 (2017).
7. U. Teğin, B. Rahmani, E. Kakkava, *et al.*, Adv. Photonics **2**, 056005 (2020).
8. L. G. Wright, D. N. Christodoulides, and F. W. Wise, Science **358**, 94 (2017).
9. U. Teğin, E. Kakkava, B. Rahmani, *et al.*, Optica **6**, 1412 (2019).
10. C. Ma, B. Gao, G. Wu, *et al.*, Opt. Lett. **50**, 5210 (2025).
11. H. Qin, X. Xiao, P. Wang, and C. Yang, Opt. Lett. **43**, 1982 (2018).
12. W. He, C. Sun, Z. Qian, *et al.*, Opt. Lett. **50**, 5618 (2025).
13. M. Qiu, M. Chen, and Z. Zhang, IEEE Photonics Technol. Lett. **33**, 1073 (2021).
14. S. Ma, B. Zhang, Q. He, *et al.*, Chin. Opt. Lett. **20**, 041403 (2022).
15. H. Zhang, J. Lu, J. Peng, *et al.*, Laser & Photonics Rev. **17**, 2300017 (2023).
16. G. Sobon, “Noise-like pulses in mode-locked fiber lasers,” in *Dissipative Optical Solitons,* M. Ferreira, ed. (Springer Nature, 2022), pp. 319–337.
17. E. Treacy, IEEE J. Quantum Electron. **5**, 454 (1969).
18. A. Chong, J. Buckley, W. Renninger, and F. Wise, Opt. Express **14**, 10095 (2006).
19. A. Chong, W. H. Renninger, and F. W. Wise, J. Opt. Soc. Am. B **25**, 140 (2008).
20. O. Ougrige, F. Bessin, C. Ciret, *et al.*, Appl. Phys. Lett. **127**, 171103 (2025).
21. Z. Wang, L. Zhan, X. Fang, and H. Luo, J. Opt. Soc. Am. B **34**, 2325 (2017).
22. S. Wabnitz, Opt. Lett. **39**, 1362 (2014).
23. X. Zhao, L. Cong, C. Zhang, *et al.*, Photonics **11** (2024).
24. N. Davoudzadeh, G. Ducourthial, Spring, and B. Q., Sci. Reports **9** (2019).

FULL REFERENCES

1. M. E. Fermann and I. Hartl, "Ultrafast fibre lasers," Nat. Phot. **7**, 868–874 (2013).
2. P. Grelu and N. Akhmediev, "Dissipative solitons for mode-locked lasers," Nat. Phot. **6**, 84–92 (2012).
3. E. Vanin, A. Korytin, A. Sergeev, *et al.*, "Dissipative optical solitons," Phys. Rev. A **49**, 2806 (1994).
4. V. J. Matsas, T. P. Newson, D. J. Richardson, and D. N. Payne, "Selfstarting passively mode-locked fibre ring soliton laser exploiting nonlinear polarisation rotation," Electron. Lett. **28**, 1391–1393 (1992).
5. Y. Meng, O. Ougrige, F. Bessin, *et al.*, "Broadband noise-like pulses in fiber laser based on a filter," Appl. Phys. Lett. **124**, 201104 (2024).
6. K. Krupa, A. Tonello, B. M. Shalaby, *et al.*, "Spatial beam self-cleaning in multimode fibres," Nat. Phot. **11**, 237–241 (2017).
7. U. Teğin, B. Rahmani, E. Kakkava, *et al.*, "Single-mode output by controlling the spatiotemporal nonlinearities in mode-locked femtosecond multimode fiber lasers," Adv. Photonics **2**, 056005–056005 (2020).
8. L. G. Wright, D. N. Christodoulides, and F. W. Wise, "Spatiotemporal mode-locking in multimode fiber lasers," Science **358**, 94–97 (2017).
9. U. Teğin, E. Kakkava, B. Rahmani, *et al.*, "Spatiotemporal self-similar fiber laser," Optica **6**, 1412–1415 (2019).
10. C. Ma, B. Gao, G. Wu, *et al.*, "All-fiber spatiotemporal self-similar laser," Opt. Lett. **50**, 5210–5213 (2025).
11. H. Qin, X. Xiao, P. Wang, and C. Yang, "Observation of soliton molecules in a spatiotemporal mode-locked multimode fiber laser," Opt. Lett. **43**, 1982–1985 (2018).
12. W. He, C. Sun, Z. Qian, *et al.*, "Noise-like pulse generation in high-power spatiotemporal mode-locked fiber lasers with 41% optical-to-optical efficiency," Opt. Lett. **50**, 5618–5621 (2025).
13. M. Qiu, M. Chen, and Z. Zhang, "Wavelength-dependent kerr beam self-cleaning in spatiotemporal mode-locked multimode fiber laser," IEEE Photonics Technol. Lett. **33**, 1073–1076 (2021).
14. S. Ma, B. Zhang, Q. He, *et al.*, "Wavelength-tunable mode-locked yb-doped fiber laser based on nonlinear kerr beam clean-up effect," Chin. Opt. Lett. **20**, 041403 (2022).
15. H. Zhang, J. Lu, J. Peng, *et al.*, "Investigation of high-power spatiotemporal mode-locking with high beam quality," Laser & Photonics Rev. **17**, 2300017 (2023).
16. G. Sobon, "Noise-like pulses in mode-locked fiber lasers," in *Dissipative Optical Solitons,* M. Ferreira, ed. (Springer Nature, 2022), pp. 319–337.
17. E. Treacy, "Optical pulse compression with diffraction gratings," IEEE J. Quantum Electron. **5**, 454–458 (1969).
18. A. Chong, J. Buckley, W. Renninger, and F. Wise, "All-normal-dispersion femtosecond fiber laser," Opt. Express **14**, 10095–10100 (2006).
19. A. Chong, W. H. Renninger, and F. W. Wise, "Properties of normal-dispersion femtosecond fiber lasers," J. Opt. Soc. Am. B **25**, 140–148 (2008).
20. O. Ougrige, F. Bessin, C. Ciret, *et al.*, "Spectral-filtering-induced phase transition in passively mode-locked fiber lasers," Appl. Phys. Lett. **127**, 171103 (2025).
21. Z. Wang, L. Zhan, X. Fang, and H. Luo, "Spectral filtering effect on mode-locking regimes transition: similariton-dissipative soliton fiber laser," J. Opt. Soc. Am. B **34**, 2325–2333 (2017).
22. S. Wabnitz, "Optical turbulence in fiber lasers," Opt. Lett. **39**, 1362–1365 (2014).
23. X. Zhao, L. Cong, C. Zhang, *et al.*, "Passively mode-locked erbium-doped fiber laser and application in laser thrombolysis," Photonics **11** (2024).
24. N. Davoudzadeh, G. Ducourthial, Spring, and B. Q., "Passively mode-locked erbium-doped fiber laser and application in laser thrombolysis," Sci. Reports **9** (2019).